INSTITUTE OF PHYSICS PUBLISHING JOURNAL OF MICROMECHANICS AND MICROENGINEERING

J. Micromech. Microeng. **15** (2005) 362–376 doi:10.1088/0960-1317/15/2/017

Microscale boiling heat transfer in a micro-timescale at high heat fluxes

Jinliang Xu[1], Yunhua Gan[1,2], Dacheng Zhang[3] and Xiuhan Li[3]

[1] Guangzhou Institute of Energy Conversion, Chinese Academy of Science, Nengyuan Road, Wushan, 510640, Guangzhou, People's Republic of China
[2] Department of Thermal and Energy Engineering, University of Science and Technology of China, Hefei, 230027, Anhui Province, People's Republic of China
[3] Institute of Microelectronics, Peking University, Beijing, 100871, People's Republic of China

E-mail: xujl@ms.giec.ac.cn

Received 16 August 2004, in final form 25 October 2004
Published 24 November 2004
Online at stacks.iop.org/JMM/15/362

Abstract

Microscale boiling heat transfer experiments were performed using acetone as the working fluid in ten parallel silicon microchannels with hydraulic diameters of 155.4 μm. An infrared radiator image system is used for the chip temperature measurements, while an optical system combining a microscope and a high-speed camera is used for transient flow pattern identification. By covering the present data range it is found that all microchannels repeat the transient flow patterns in a timescale of milliseconds while the fluid pressures/temperatures are stable. A full cycle can be subdivided into three substages: liquid refilling stage, bubble nucleation, growth and coalescence stage, and transient annular flow stage. Correspondingly four flow patterns are identified. Paired or triplet bubbles are observed to be nucleated and grow up simultaneously in, or very close to, the channel corners at the same cross section. The nucleated bubbles experience several milliseconds of growth until coalescence takes place. Then a single liquid plug is separated into two parts, which are pushed out of the flow field view in less than 1 ms. In the transient annular flow stage, the liquid films that are drawn into the corners of the channel become less and less versus time. Once a partially or fully dried-out state is reached, all the microchannels are refilled with fresh liquid and a new cycle begins. The probabilities of each flow pattern occurring and the liquid refilling follow the statistical principle well. The measured chip temperatures are not uniform across the whole heating area, attributed to the uneven liquid refilling probabilities for different channels and the uneven possibilities that are immersed in the liquid for different heating regions. The chip temperatures display spatial variation behavior in the majority of the heating area, due to the liquid and vapor alternatively passing through the microchannels. To the authors' knowledge, some of the above experimental findings have not been previously reported.

Nomenclature

b	side wall width of the triangular microchannel (m)
C_p	specific heat (J kg^{-1} K^{-1})
D_h	hydraulic diameter of the microchannel (m)
G	mass flux (kg m^{-2} s)
h_{fg}	latent heat of evaporation (J kg^{-1})
$h(z, y)$	two-dimensional heat transfer coefficient in z and y coordinates (W m^{-2} K^{-1})
I	current passing through the heater (A)
k	thermal conductivity (W m^{-1} K^{-1})
L_h	effective heating length (m)

L_{sp}	length for the single-phase liquid flow based on the mean energy conservation principle (m)
m	mass flow rate (kg s^{-1})
N	total number of microchannels
p_{in}	inlet pressure (bar)
p_{sat}	saturated pressure of the fluid (bar)
q	effective heat flux based on the side wall channel area (W m^{-2})
Q	effective heating power (W)
Re	liquid Reynolds number
t	time (s)
T	temperature (°C)
$T_f(z)$	liquid temperature along the flow length direction (°C)
$T_w(z, y)$	two-dimensional chip temperatures in z and y coordinates (°C)
U	inlet liquid velocity (m s^{-1})
V	voltage applied on the heater (V)
W	width of the heater (m)
$x(z)$	vapor mass quality along the flow length direction
x_e	mean exit vapor mass quality
y	the coordinate for the heater width direction (m)
z	the coordinate along the flow length direction (m)

Greek symbols

Δp	pressure drop over the microchannels (Pa)
ρ	density (kg m^{-3})
σ	surface tension (N m^{-1})
ν	kinematic viscosity (m^2 s^{-1})
μ	viscosity (Pa s)
φ	the ratio of heat transfer to the working fluid to the total heating power

Subscripts

f	liquid state
g	vapor state
in	inlet condition
sat	saturated condition

1. Introduction

Recently, great attention has been paid to phase-change flow and heat transfer at the microscale size, either using silicon or copper microchannel heat sinks, due to its effective heat transfer performance as compared with single-phase liquid flow in microchannels [1]. However, safe operation of the high heat flux microchannel heat sink with boiling heat transfer inside requires a better understanding of the complicated flow and heat transfer mechanism. Designing a microchannel heat sink involves many issues such as flow patterns, pressure drops, heat transfer coefficients, critical heat fluxes and flow instabilities. These topics were reviewed by Kandlikar [2, 3] and Thome [4].

Understanding two-phase flow patterns at microscales is very helpful in designing effective compact boiling/condensation heat exchangers with a characteristic channel size of less than 1 mm. Many studies deal with air–water two-phase flow patterns in capillary tubes or channels with hydraulic diameters of about 1 mm. Some examples include Kawahara *et al* [5], Chen *et al* [6], Zhao and Bi [7], Triplett *et al* [8], Feng and Serizawa [9] and so on.

Few studies were performed for the boiling two-phase flow patterns with a characteristic channel size of much less than 1 mm, which should be distinct from the air–water two-phase flows in microtubes or channels. A recent literature survey demonstrates that the complicated boiling two-phase flow patterns in microchannels may result in flow instabilities [10–14].

Jiang *et al* [10] conducted microscale boiling heat transfer in triangular silicon microchannels for hydraulic diameters of 26 μm and 53 μm. They found that there are fewer nucleation sites at low heating powers. At moderate heating powers, flow patterns change to an unstable slug flow that was forced through the microchannels, completely suppressing the remaining active nucleation sites. At the higher heating power range, a stable annular flow mode was developed, with a clear vapor/liquid interface with no liquid droplets in the vapor core.

Peles *et al* [11] performed experiments in silicon microchannels and developed a mathematical model that divides the whole flow field into a liquid part and a vapor part. The model consists of a set of non-dimensional parameters. The findings show that a mean outlet vapor mass quality less than unity represents the liquid and the vapor phase (not the vapor/liquid mixture) passing through the channel exit alternately.

Hetsroni *et al* [12] used three microchannel heat sinks with hydraulic diameters of 129 μm, 103 μm and 161 μm. The experimental results showed that the low heat flux region is characterized by the presence of a liquid phase in part of the microchannels. The mean chip temperature is less than the saturation temperature of the fluid. The high heat flux region is characterized by convective boiling, in all parallel microchannels, accompanied by quasi-periodic rewetting and refilling of the microchannels. In such a study, incorporating the experimental studies reported in Hetsroni [15], it was found that the pressure drops and exit fluid temperatures display periodic oscillations with a cycle period in the order of seconds (1–2 s). The parameter oscillations were attributed to the bubble growth and collapse of the vapor fraction.

Wu and Cheng [13] studied the boiling two-phase flow instabilities in silicon microchannels. They found large amplitude/long period oscillations and such instabilities were noted to be self-sustained if the pressure drop and the mass flux are out of phase. The long oscillation cycle periods can be up to the order of 10 to 100 s. Xu *et al* [14] measured the onset of flow instability (OFI) (static flow instability) and dynamic flow instability using 26 rectangular microchannels each with a width of 300 μm and a depth of 800 μm, using deionized water as the working fluid. The onset of flow instabilities was identified as occurring at the outlet temperature of 93–96 °C, which is several degrees lower than the saturated temperature corresponding to the exit pressure. Once the mass flux is lower than that at the OFI condition, three types of flow instability were identified: large amplitude/long period superimposed with small amplitude/short period oscillation, small amplitude/short period oscillations. Thermal oscillations of the microchannel wall temperatures always accompany the above two oscillations. The reported cycle periods are also very long.

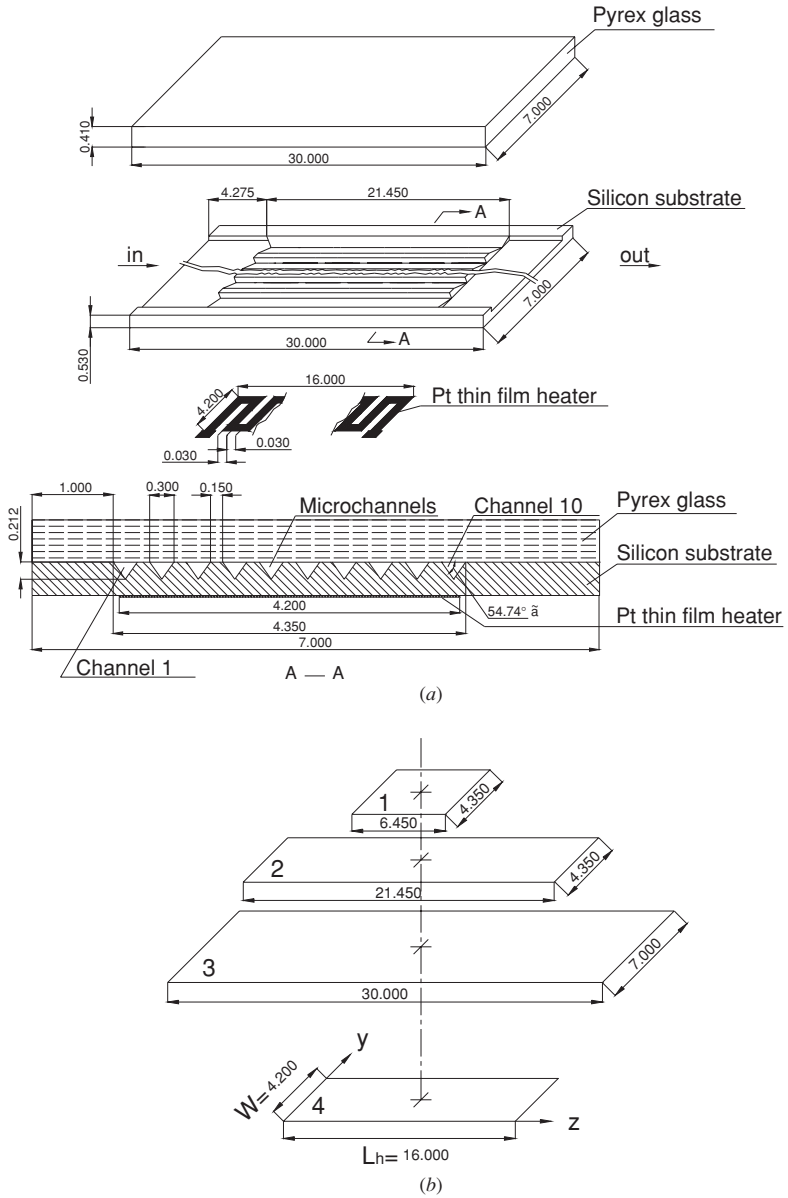

Figure 1. Silicon microchannel test section. 1: Flow view field; 2: microchannels area; 3: whole silicon chip; 4: effective thin film heater (all dimensions are in mm).

In this paper, we performed the boiling two-phase flow experiment in ten parallel triangular microchannels at high heat fluxes using two optical systems, one is a infrared radiator (IR) system for the chip temperature measurement, the other is a system combing a microscope and a high-speed camera, and found the following. (1) All microchannels repeat the transient flow patterns in milliseconds. (2) A full cycle can be divided into three substages: liquid refilling stage, bubble nucleation, growth and coalescence stage, transient annular flow with decreased liquid film thickness versus time stage. (3) Paired or triplet bubbles are observed to be nucleated and grow up simultaneously in, or very close to, the channel corners of the same cross section. (4) Once paired or triplet bubbles are merged at a specific cross section, a single liquid plug is separated into two parts, which are pushed quickly out of the flow field view. Then soon the microchannels are without liquid and move to the transient liquid film evaporation for annular flow stage. (5) The transient boiling two-phase flow patterns result in an uneven chip temperature versus space location, which is distinct from what we imagined for boiling two-phase heat transfer.

2. Description of the experiment

2.1. Microchannel heat sink

A silicon multi-microchannel heat sink was designed and fabricated in the typical clean room environment, as shown in figure 1. The silicon wafer is 30 mm long, 7 mm wide and 530 μs thick. Ten parallel triangular microchannels, which were centrally located in the silicon substrate with the total length of 21.450 mm and the total width of 4.350 mm, were etched. The cross section of each triangular microchannel has a width of 300 μm and a depth of 212 μm, forming a hydraulic diameter of 155.4 μm. The angles at the base are

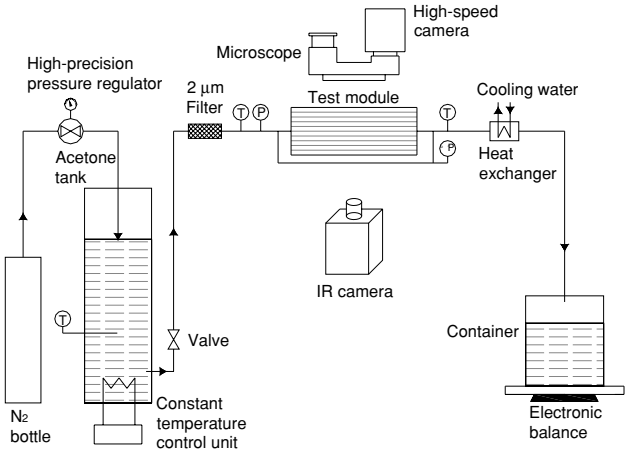

Figure 2. Schematic diagram of the experimental set-up.

54.74°. The pitch between two triangular microchannels is 150 μm. A Pyrex glass cover, 410 μm thick, served as both an insulator and a transparent cover through which flow patterns and boiling phenomenon could be observed.

On the back of the silicon wafer, a thin platinum film was deposited by the 'chemical vapor deposition' technique to provide a uniform heat flux. The length of the thin film is exactly the same as that of the longitudinal microchannels, 21.450 mm. In order to ensure the safe operation of the microchannel heat sink, the width of the thin platinum film is kept to 4.200 mm, which is narrower by half a triangular microchannel width than the total microchannel width. The effective heating length of the thin film is 16.000 mm, centrally located about the wafer. The optical flow field view is 6.450×4.350 mm^2 for the flow pattern identifications, which covers the whole microchannel width, but covers only 40% of the total heating length (6.450 mm relative to 16.000 mm), which has larger flow field view than those of other studies. The relative positions of the flow field view, the parallel microchannels, the whole silicon chip and the thin platinum film are illustrated in figure 1(*b*). The *y*–*z* coordinates are attached on the effective thin film heater, with the *y*-coordinate for the channel width direction and the *z*-coordinate for the axial flow direction (see figure 1(*b*)). The total effective thin film heating area (16.000×4.200 mm^2) is the area for the IR image temperature measurements. A precision ac power supply unit drives the thin platinum film. The heat generated in the heater was transferred to the fluid flow from the microchannels.

2.2. Experimental set-up

The experimental apparatus, schematically shown in figure 2, consisted of the following subsystems: (1) external fluid-handling system; (2) silicon microchannel heat sink; (3) high-speed data acquisition system; (4) infrared radiator image system; (5) optical system incorporating a microscope and a high-speed camera.

2.2.1. External fluid-handling system. The fluid-handling system is composed of a high-pressure nitrogen gas bottle, a pressurized liquid tank, a 2-micrometer filter, a heat exchanger and a liquid collector. Connection tubes, tube adaptors and valves join each hardware piece together. The liquid acetone is pressurized by the high-pressure nitrogen gas and successively flows through the liquid valve, the filter, the silicon wafer test section, the heat exchanger and is collected in the liquid container. A high-precision pressure regulator valve at the top of the nitrogen gas bottle was used to adjust the upstream pressure of the microchannel test section. At the bottom of the pressurized liquid tank an electronic heater was arranged to control the liquid temperature using a constant temperature control unit (PID) with an uncertainty of 0.5 °C. A thick insulation material was wrapped around the connection tube to decrease the heat loss to the environment. The heat exchanger was used to condense the hot two-phase mixture from the microchannel heat sink. Thus the liquid (not the liquid/vapor mixture) can be collected in the container. The mass flow rate was measured by the increased mass in the liquid container over a long period of time using a high-precision electronic balance, which has an uncertainty of 0.002 g. The inlet/outlet temperatures of the microchannel heat sink were measured by two high-precision jacket thermocouples, which were located at the centerline of the connection tubes, having the errors of 0.2 °C after calibration with a constant temperature bath. The inlet pressure was measured by a Setra pressure transducer (model 206), which has an uncertainty of 1% after calibration with a known standard. A Senex differential pressure transducer was installed across the microchannel heat sink to measure the pressure drop: uncertainty is 0.1%. The fluid temperatures, pressure sensors and differential pressure transducers have the response time of 0.2 s, 0.1 s and 0.01 s respectively. These signals were collected by an HP high-speed data acquisition system and displayed by a PC monitor and stored in the PC memory for further analysis.

2.2.2. Infrared radiator image system. A high-resolution, high-accuracy infrared radiator imaging system (FLIR ThermaCAM SC3000 IR) measures the thin Pt film temperature on the back of the silicon wafer. The thermal sensitivity at the room temperature is 0.02 °C with a spatial resolution of 1.1 mrad, a typical resolution of 320×240 pixels over the whole heating area, and an image frequency of 50 Hz. The above parameters of the IR image system ensure the precise determination of the temperature gradients over the chip surface. The fraction of the focused field length viewed by the IR camera relative to that of all microchannels is 74.6%, but covers the whole microchannel width. The relative positions are shown in figure 1(*b*).

For all the tests, the IR camera was focused on the heating area of the silicon wafer (16.0×4.2 mm^2). The temperature gradient and the maximum wafer temperature could be measured for different power levels. The variations in the maximum chip temperature and the transient response were also readily detected. The IR image was displayed on a PC screen and stored in the PC memory for further analysis. A total of 6080 data points corresponding to the focused thin film heating area were stored in an Excel file for each run.

The measurement principle using the radiation power emitted from a surface requires careful calibration of the emissivity. The surface topography and the wavelengths

Table 1. Physical properties of acetone at 1 bar saturated condition.

T_{sat} °C	ρ_f (kg m^{-3})	C_{pf} (J (kg^{-1} °C^{-1}))	C_{pg} (J (kg^{-1} °C^{-1}))	h_{fg} (J kg^{-1})	σ (N m^{-1})	μ_f (Pa s)	μ_g (Pa s)	k_f (W (m^{-1} °C^{-1}))	k_g (W (m^{-1} °C^{-1}))
56.29	748.01	2302.5	1380.6	512.94	0.0192	2.37×10^{-4}	8.31×10^{-6}	0.518	0.0136

that are interrogated strongly affect the emissivity [16]. The spatial resolution is limited by diffraction to the order of the wavelength contribution to the sensitivity. A very thin 'black lacquer' was uniformly coated on the thin film surface. An emissivity of approximately 0.94 resulted in a good measurement with an accuracy of 0.4 °C after calibration with a high-precision thermocouple over the temperature range of 30 °C to 100 °C. The temperature dependence of the emissivity within the considered range can be neglected. Such a procedure is similar to that of Hapke *et al* [17].

2.2.3. Optical system including the microscope and the high-speed camera. The microscope is a Leica M Stero-microscope (Germany), with a total enlargement factor of 183. During the measurement, a cold light source was turned on to form a clear image on the PC screen. The microscope can be used independently. However, for the present applications, a high-speed camera system was connected with the microscope through a 1 inch C-type port. The HG-100K (Redlake Inc., USA) high-speed camera was used with an advanced 1.7M CMOS sensor, which can capture dynamic pictures up to 20000 frames/s, with the resolution of 1504 × 1128 pixels. However, a very high recording rate, such as more than 5000 frames/s, requires a very powerful light source. Due to the explosive bubble growth phenomenon observed, a high recording rate of 1000 or 2000 frames/s was used.

2.3. Experimental procedure

The present experimental procedure is as follows.

(1) Close all of the valves in the system.
(2) Open and adjust the pressure-regulating valve at the top of the nitrogen gas tank to the desired pressure value.
(3) Put the heat exchange into operation.
(4) Open the related valves of the flow system and establish the flow.
(5) Adjust the pressure valve and fix the inlet pressure of the microchannels. Because the exit of the microchannels is exposed directly to the environment, the pressure drop over the microchannel heat sink is also given and corresponds to the inlet pressure.
(6) Turn on the heating power to a desired value.
(7) Leave the system unchanged for 30 min until it is stable. Record the pressures and fluid temperatures using the high-speed data acquisition system. The optical system records the dynamic flow patterns. Generally, the recording time is 2–3 s at the recording rate of 1000 or 2000 frames per second. The recording time consists of 20 to 100 full cycles. The IR image system records the chip temperature file.
(8) The electronic balance records the mass increment over a given period of time and obtains the mass flow rate.
(9) Once a run is over, increase the heating power to another value and repeat the process from 6 to 8.
(10) For a given pressure drop, the heating power is increased from lower value to a very high value step-by-step, until the maximum chip temperature reaches around 100 °C. Switch the system to a higher inlet pressure of the microchannel and repeat the process from 5 to 9.

The present experiment covers the following parameter ranges: pressure drops over the microchannels from 30 to 60 kPa, inlet liquid temperatures around 30 °C, heat fluxes from 50 to 500 kW m^{-2}. The corresponding mass fluxes varied from 50 to 1200 kg m^{-2} s^{-1}.

2.4. Data reduction

2.4.1. Physical properties. We use the pure liquid acetone (CH_3COCH_3, molecular weight of 58.08, purity >99.5%) as the working fluid. Its physical properties are listed in table 1 at 1 bar saturated condition [18].

In table 1, T_{sat} is the saturated temperature, ρ_f is the liquid density, C_{pf} and C_{pg} are the specific heat of the liquid and vapor, σ is the surface tension force, μ_f and μ_g are the liquid and vapor viscosities, k_f and k_g are the thermal conductivities of the liquid and vapor.

The saturated pressure and the temperature have the following relationship,

$$P_{sat} = 133.3 \times 10^{(23.5884-2.4690\times10^3/(T+273.15)-7.3510 \times \log_{10}(T+273.15)+2.8025\times10^{-10}\times(T+273.15)+2.7361\times10^{-6}\times(T+273.15)^2)} \quad (1)$$

where p_{sat} and T are the saturated pressure and temperature and have the units of bar and °C.

The liquid specific heat and the latent heat of evaporation can be computed as

$$C_{pf} = (1000/58.08) \times (46.878 + 0.626\,52 \times (T + 273.15) - 2.0761 \times 10^{-3} \times (T + 273.15)^2 + 2.9583 \times 10^{-6} \times (T + 273.15)^3) \quad (2)$$

$$h_{fg} = (1000/58.08) \times 49.244 \times (1 - (T + 273.15)/508.2)^{0.481} \quad (3)$$

where C_{pf} and h_{fg} have the units of J kg^{-1} K^{-1} and J kg^{-1} respectively. Other mathematical expressions for the acetone liquid and vapor are also available from [18].

2.4.2. Heat flux, q. Heat loss to the environment due to conduction, convection and radiation was taken into account. The net heat flux was defined as $q = \varphi V I/(2NbL_h)$, where V and I are the voltage and current applied on the heater, N is the total number of the microchannels, b and L_h are the side wall width of the triangular microchannel and the effective heating length of the heater and φ is the ratio of the heat

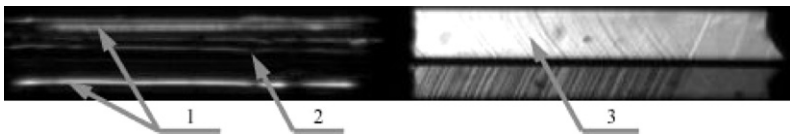

Figure 3. Air–water calibration result in a single microchannel. 1: Liquid film in the corner; 2: gas core (air); 3: liquid plug.

transfer to the working fluid to the total heating power. Before the two-phase experiment, the single-phase liquid flow was established, φ was determined by the energy balance in terms of the measured inlet and outlet temperatures [12].

2.4.3. Reynolds number. $Re = U D_h/\nu$, where U is the mean flow velocity of the single-phase liquid, D_h is the hydraulic diameter of the microchannel and ν is the liquid kinematic viscosity at the inlet collector. The mass flow rate m is computed from the increased liquid mass over a given period of time. The vapor mass quality at the exit plenum, x_e, was computed from the energy conservation equation in terms of the enthalpy increase from the inlet to the outlet.

2.4.4. Two-dimensional heat transfer coefficient. Corresponding to the measured temperature field of the focused thin film heating area, two-dimensional heat transfer coefficients were obtained related to the axial flow direction (z-direction) and its perpendicular direction (y-direction). The whole focused effective heating area is divided into two regions: the single-phase liquid flow region and the two-phase flow region. The single-phase liquid flow length, L_{sp}, is computed in terms of the energy conservation,

$$L_{sp} = mC_{pf}L_h(T_{\text{sat}} - T_{\text{in}})/Q \tag{4}$$

where Q is the effective heating power. In the liquid flow region, the linear liquid temperature distribution along the flow length is assumed. The liquid temperature ($T_f(z)$), local vapor mass quality ($x(z)$) and the heat transfer coefficient ($h(z, y)$) were calculated as

$$T_f(z) = T_{\text{in}} + \frac{z}{L_{sp}}(T_{\text{sat}} - T_{\text{in}}) \tag{5}$$

$$x(z) = \frac{C_{pf}(T_{\text{in}} - T_{\text{sat}}) + \frac{z}{L_h}\frac{Q}{m}}{h_{fg}} \tag{6}$$

$$h(z, y) = \frac{q}{T_w(z, y) - T_f(z)}. \tag{7}$$

Note that $x(z)$ is negative in the liquid flow region and $T_w(z, y)$ is the local chip wall temperature measured by the IR image. In the two-phase region, the vapor mass quality is positive in equation (6). The liquid temperature is replaced by the constant saturated temperature T_{sat} related to the saturated pressure, which is incorporated into the calculation of the local heat transfer coefficients in equation (7).

3. Results and discussion

3.1. Air–water flow calibration of the optical system

In contrast to other studies, our optical system (the microscope connected to the high-speed camera) identifies the gas phase as 'black' image and liquid phase as 'white' image. Before performing the boiling two-phase flow in microchannels, we performed the simple air–water two-phase flow to identify the image characteristics. Initially, the microchannels are filled with air because they are connected to the environment through the connection tubes. Then the liquid water is pushed slowly into the microchannels. Figure 3 illustrates a typical image using one channel instead of ten. The flow direction is from left to right (this is true for all of our experiments), with the liquid plug as white image and the bubble slug as black image. The gas/liquid interface is flat. The white straight line in figure 3 is the liquid film drawn to the microchannel corners due to the surface tension effect.

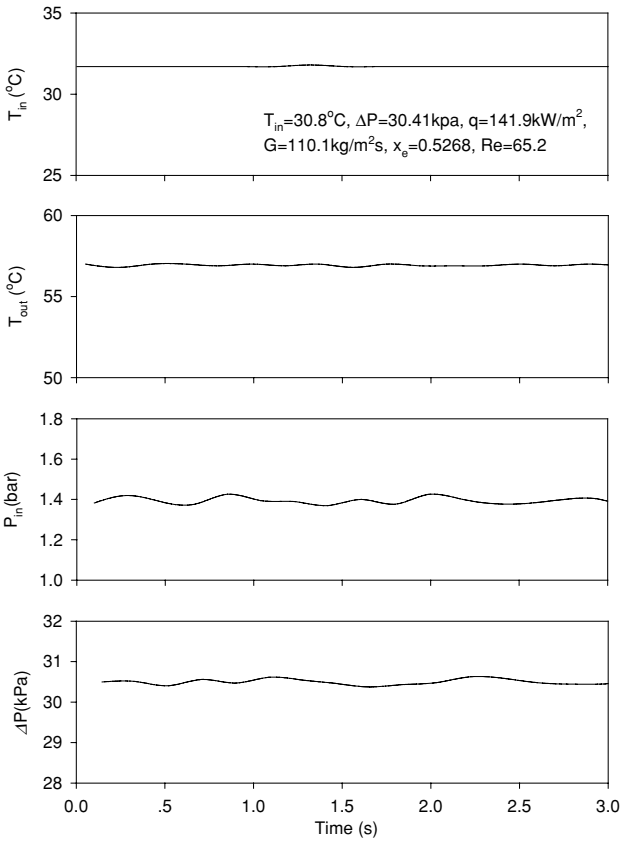

Figure 4. Quasi-stable fluid pressure, pressure drop and temperature output versus time.

3.2. Transient flow patterns and boiling phenomenon at moderate exit vapor mass quality

The present study identifies the smooth fluid pressure/temperatures versus time, as shown in figure 4. The operation parameters are as follows: the inlet liquid temperature of 30.8 °C, the pressure drop across the microchannels of 30.41 kPa, the heat flux of 141.9 kW m^{-2}, the mean outlet

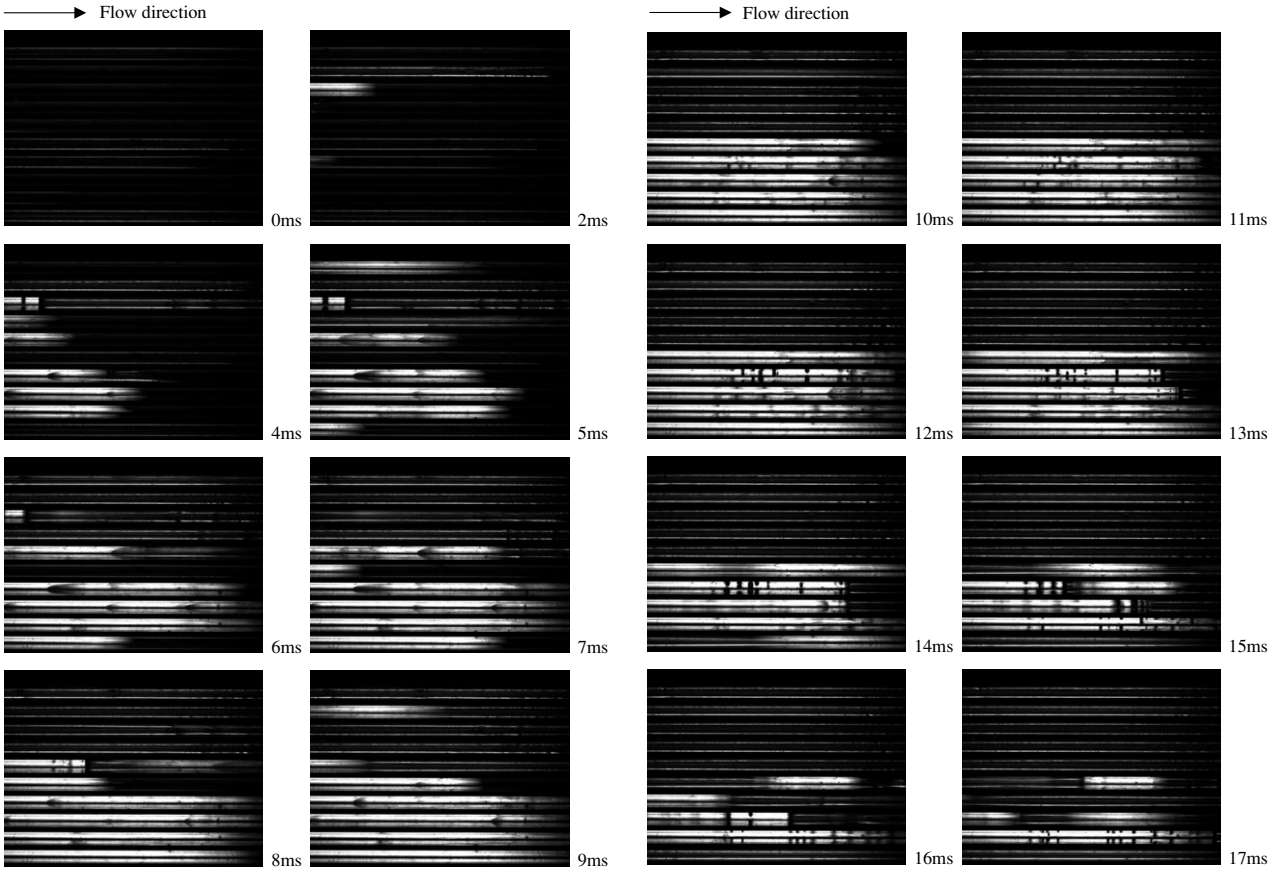

Figure 5. Transient flow patterns in all microchannels for a full cycle.

Figure 5. (Continued.)

vapor mass quality of 0.5268 and the liquid Reynolds number of 65.2. All microchannels repeat the transient flow patterns periodically in milliseconds (see figure 5). The cycle period is 47 ms for such run. Figure 6 shows the four typical flow patterns: (1) flow pattern A, liquid plug/vapor slug flow, (2) flow pattern B, inverse bubble slug entrained in the liquid plug flow, (3) flow pattern C, paired or triplet bubbles entrained in liquid plug, (4) flow pattern D, transient annular flow. The four flow patterns occur in the microchannels alternately for successive cycles. The probability of appearance is defined as the occurring time of each flow pattern divided by the cycle period. The subparts in figure 6, obtained for eight successive cycles, show that the probabilities of appearance satisfy the statistic principle. The probability of appearance is increased from pattern A to pattern D. Flow pattern A has the smallest probability of appearance while flow pattern D has the largest probability of appearance. It is seen that the transient flow repeats the process well in cycle behavior. The reason why the pressures/fluid temperatures are stable versus time is because the cycle period of the transient flow patterns is so short and in the same order or even shorter than the response time of the pressure/fluid temperature sensors. Thus these electronic sensors cannot track the fast transient flow patterns inside microchannels. In addition to this, the parallel microchannels may also even out the sensor's output versus time.

It is noted that two-phase flow instabilities were also reported in [12–14]. These studies demonstrated that the fluid pressures/temperatures vary versus time accompanying the periodic variations of the two-phase flow patterns with the cycle period in seconds or even longer. To the author's knowledge, analysis of these flow instabilities may need to incorporate the effect of the external fluid-handling system, such as the upstream compressible volume, the connection tubes and so on. The transient flow patterns in all microchannels, in milliseconds, with the constant fluid pressure/temperatures are governed by the unconventional flow and heat transfer mechanism in microchannels, which may not be related to the external fluid-handling system.

3.2.1. Description of the transient flow patterns in a single or all microchannels. A full cycle starts from the nearly dried-out state and returns to such state when a cycle period elapses. It can be divided into three substages (see figure 5): liquid refilling stage ($0 < t < 9$ ms), bubble nucleation, coalescence and explosion stage (10 ms $< t < 21$ ms), and transient liquid film evaporation stage (22 ms $< t < 47$ ms). The image at $t = 0$ is the last one for the end of the previous cycle at which the whole flow field view is black, indicating the nearly dried-out state in the microchannels, but with some horizontal white lines, representing the liquid films that were drawn to the triangular channel corners due to the surface tension effect.

Liquid refilling stage ($0 < t < 9$ ms *in figure 5).* Liquid plugs refill some of the microchannels, represented by the white image. For most of the microchannels, only one liquid plug

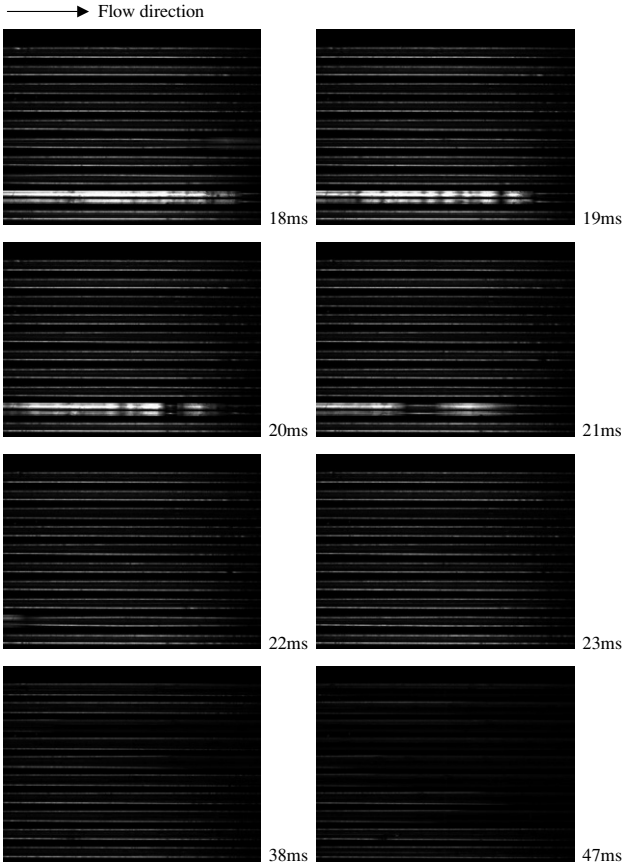

Figure 5. (Continued.)

enters the microchannel with the normal traveling speed of the vapor/liquid front, separating the corresponding microchannel into the liquid plug region and the vapor slug region (flow pattern A in figure 6). The vapor/liquid interface is sometimes flat. However, for some of the microchannels, two liquid plugs are observed traveling from left to right with a short distance in between. It is also observed that some liquid plugs may entrain the 'inverse bubble slug' (flow pattern B in figure 6), which is so named because it is the opposite to the conventional vapor slug. Thome [19] proposed the transient liquid film model based on a set of elongated bubble slugs in each microchannel. The proposed elongated bubble slug has the protruding advancing vapor/liquid interface, but has the flat receding interface. A short liquid bridge is maintained between two neighboring bubble slugs. The proposed shape of the elongated bubble comes from the experimental observations of the air–water two-phase flow in microchannels. A comparison of the present bubble slug entrained in the liquid plug pattern (flow pattern B) with the elongated bubble for the air–water microchannel flow is shown in figure 7.

The bubble slug entrained in the liquid plug may be coming from the bubble nucleation, growth and coalescence ahead of the flow field view. The tail of the entrained bubble slug is stationary or moving at a very small velocity.

Heat transfer in this substage for all microchannels consists of two mechanisms: the single-phase liquid forced convection mechanism corresponding to the liquid plug traveling in part of the microchannels, and the transient liquid film evaporation mechanism corresponding to the region that is still covered by the high quality vapor. It is noted that for a full cycle, not all the microchannels are flushed by the refilling liquid. This issue will be discussed later.

*Bubble nucleation, growth, coalescence and vapor explosion stage (*10 ms $< t <$ 21 ms *in figure 5).* It is interesting to note that the paired or triplet miniature bubbles are nucleated simultaneously in, or very close to, the channel corners at the same cross section. Such a phenomenon was identified in the successive images at $t = 10$–21 ms in figure 5 and as the flow pattern C in figure 6, in which a set of bubble group train was seen, each bubble group has three spherical bubbles located at the same cross section, each bubble corresponds to one of the channel corners. The active nucleation sites are rare and the rough estimation of these sites is around 78 in the selected flow field view. Generally, once the nucleation sites at the same channel cross section gestate miniature bubbles, they will have several milliseconds to grow, before they coalesce to occupy the whole channel cross section. The explosive bubble coalescence at the specific cross section separates the single liquid plug into two parts, which are pushed quickly downstream and upstream out of the flow field view in a couple of milliseconds. Because of this, all microchannels are soon without liquid and the transient flow moves to the next substage.

On the basis of our observations, it is concluded that heterogeneous (not homogeneous) nucleation dominates the process. The presence of a small quantity of dissolved gas in the liquid may not trigger the bubble nucleation. Also, for smooth silicon microchannels, the sizes of the cavities on the channel walls are small so that they may inhibit bubble nucleation. The reason why a group of triplet bubbles appears in, or close to, the same channel cross section is explained as (1) the three channel corners have the same configurations and (2) the liquid in the three channel corners has the exact temperatures and flow velocities in these local areas.

Once the triplet bubbles merge together, the higher liquid temperatures caused by the higher wall superheat result in a sudden release of energy from liquid into the merged bubble, leading to a rapid increase in internal pressure, pushing the liquid parts quickly out of the flow field view.

It is the top view through the transparent cover that captures the dynamic flow patterns inside the microchannels. The schematic diagram of the side view of the bubble nucleation, growth and coalescence process is shown in figure 8 based on the top-view observations: figure 8(*a*) shows the initial bubble nucleation in the corners, figure 8(*b*) shows the bubble growth and figure 8(*c*) the merged bubble status. During bubble growth and coalescence, the metastable superheated liquid releases energy to the vapor, causing a sharp pressure increase inside the merged bubble thus moving the separated liquid parts quickly downstream and upstream of the microchannels.

Figures 9–11 are examples showing bubble nucleation, growth and coalescence for a single microchannel, noting that the definition of the time sequence is different from that for all microchannels. The successive images are selected as in figure 5, but for a different cycle (not included in figure 5).

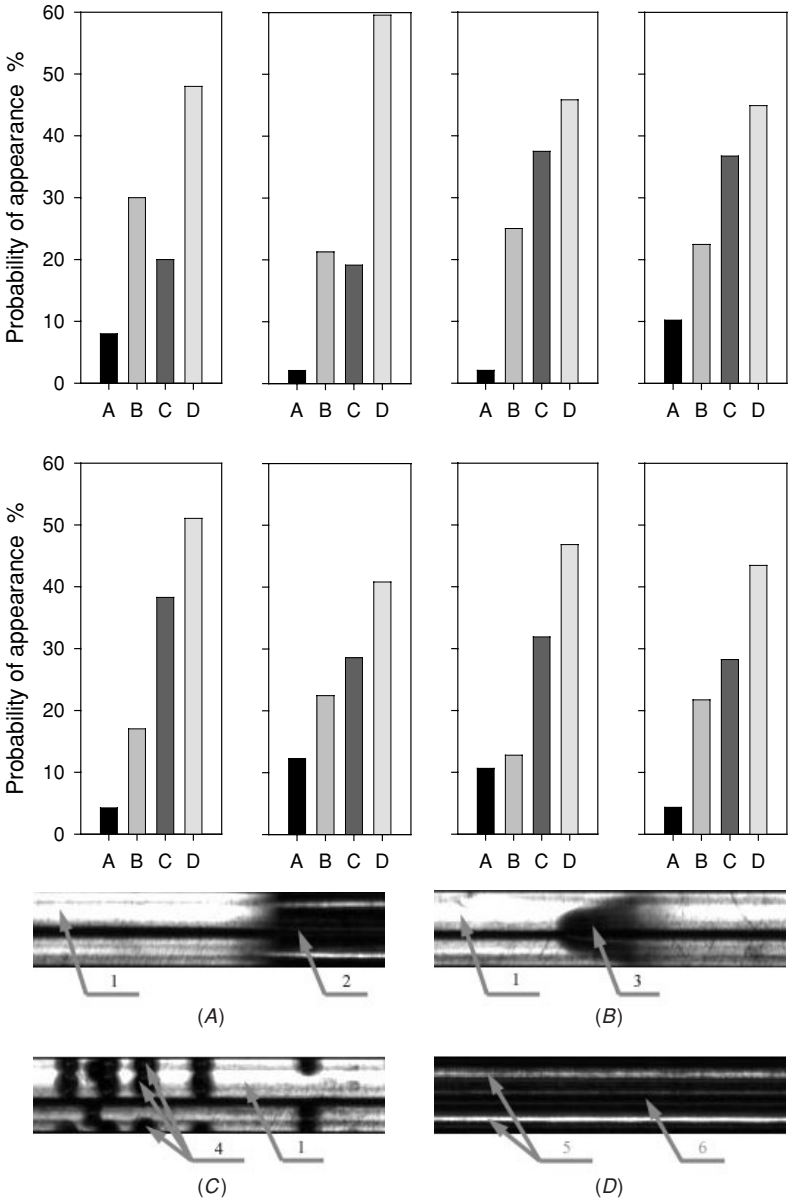

Figure 6. Probability of the appearance of different flow patterns for successive cycles. (*A*) Liquid plug/vapor slug flow; (*B*) bubble slug entrained in a liquid plug; (*C*) bubbles entrained in a liquid plug; (*D*) annular flow. 1: liquid plug; 2: vapor slug; 3: bubble slug; 4: triplet spherical bubbles; 5: liquid film in the corner; 6: vapor core.

In figure 9, at $t = 3$ ms, a set of bubble groups appeared. Each group has two or three bubbles, symmetrically located at the same cross section. At $t = 5$ ms, the liquid plug A is separated by the merged bubble in the cross section A, which is pushed out of the flow view field to the channel outlet at $t = 6$ ms. Meanwhile, the liquid plugs B and C are separated by the merged bubble in cross section B. The two liquid plugs B and C are flushed out of the flow field view and totally disappear at $t = 7$ ms. From above, one knows that the separated liquid plugs are pushed out of the microchannels in less than 1 ms. Because the process undergone is very fast, future study needs to use a much higher recording rate to capture the bubble explosion phenomenon.

Figure 10 shows a comparison of the normal vapor/liquid front traveling velocity for $0 < t < 9$ ms and the fast traveling velocity pushed by the merged bubble which is located ahead of the flow field view. The fast vapor/liquid front traveling velocity is 1.7 m s^{-1}, which is nearly three times of the normal vapor/liquid interface traveling speed of around 0.5 m s^{-1}. The positive velocity means that the liquid plug is moving downstream. Another set of successive images showing the flow reversal caused by the merged bubbles is given in figure 11. The liquid plugs A and B are separated by the merged bubbles at $t = 12$ ms. The liquid plug A travels downstream and goes out of the flow field view at $t = 13$ ms, leaving the liquid plug B flowing back to the channel inlet for $t > 13$ ms with the speed of 1.4 m s^{-1}. The negative velocity represents the flow reversal to upstream of the microchannels.

Bubble nucleation, growth and coalescence processes are influenced by a lot of factors. A few high-speed flow visualizations were performed for the boiling two-phase flow in silicon microchannels, which have smoother

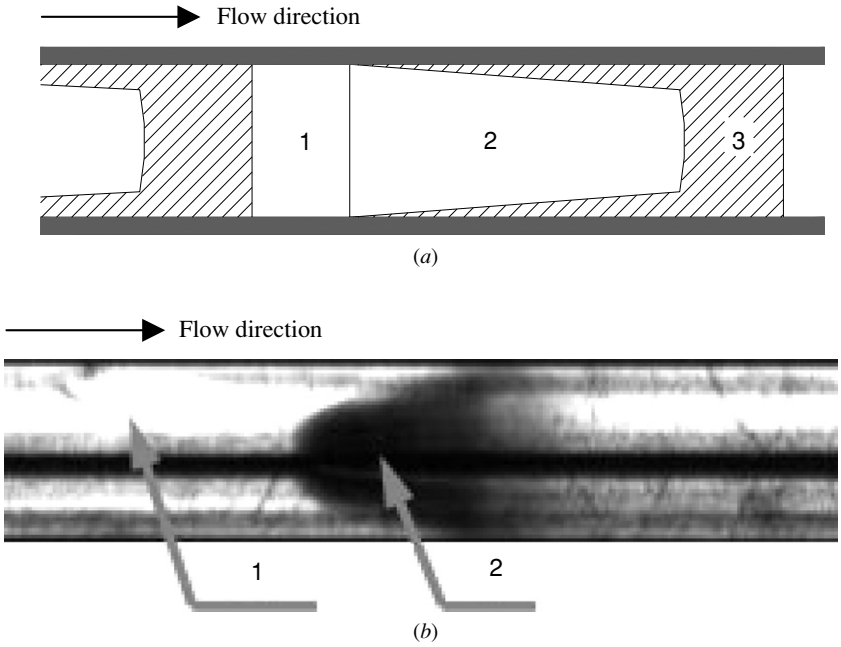

Figure 7. Comparison of the flow pattern B in the present study and the elongated bubbly flow by Thome [19]. (*a*) 1: dry zone; 2: elongated bubble; 3: liquid slug; proposed by Thome [19]. (*b*) 1: liquid plug; 2: bubble slug entrained in liquid plug (identified by the present study).

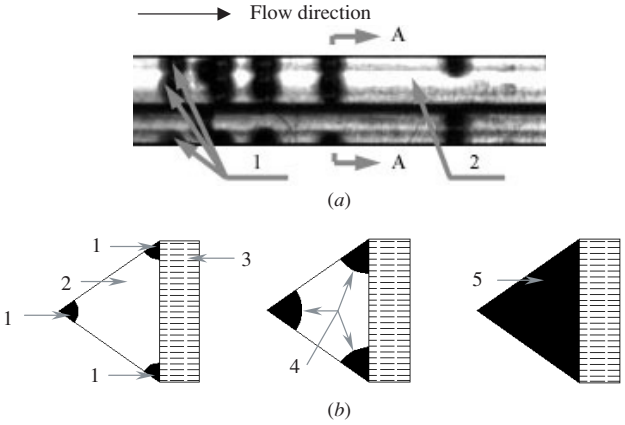

Figure 8. Bubble nucleation, growth and coalescence mechanism. (*a*) Top view observations; (*b*) A–A side view; 1: bubbles; 2: liquid; 3: glass cover; 4: energy released from the metastable superheated liquid to the vapor phase; 5: vapor occupied in the whole cross section of the microchannel.

wall roughness compared with the copper microchannel heat sinks. Peng and Wang [20, 21] performed the experiments in rectangular stainless steel microchannels with dimensions of 0.6×0.7 mm^2 using water as the working fluid. No bubbles were observed and the concepts of 'evaporating space' and 'fictitious boiling' were proposed. Qu and Mudawar [1] measured the boiling incipience for the copper microchannel heat sink and found that a small number of bubbles were observed close to the exit of the microchannels. The heat flux and the wall superheat at the boiling incipience are increased by increasing the inlet velocities and decreasing the inlet temperatures. Hetsroni *et al* [12] performed the high-speed flow visualizations in parallel silicon microchannels

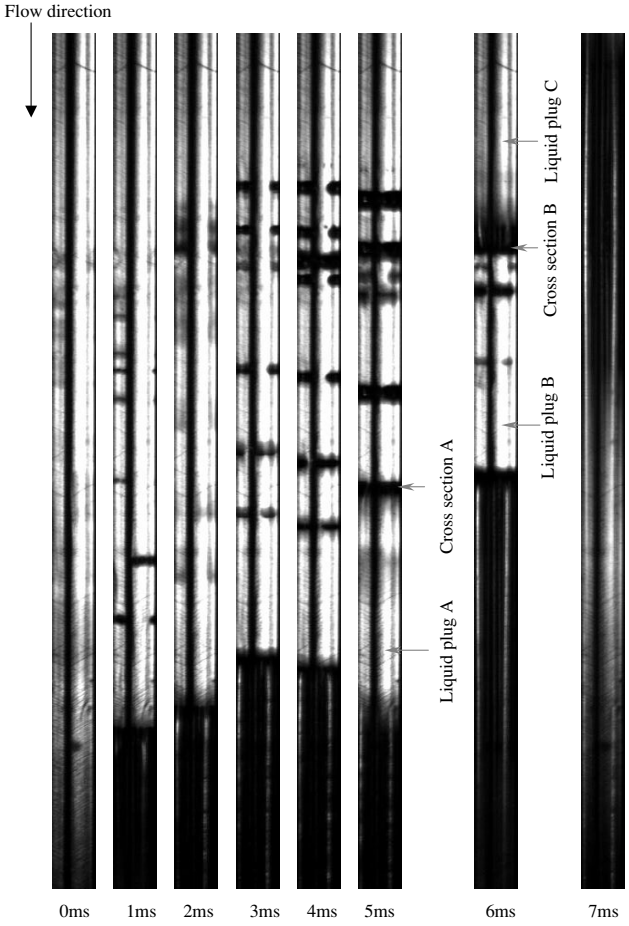

Figure 9. Bubble nucleation, growing up and coalescence sequences for channel 9.

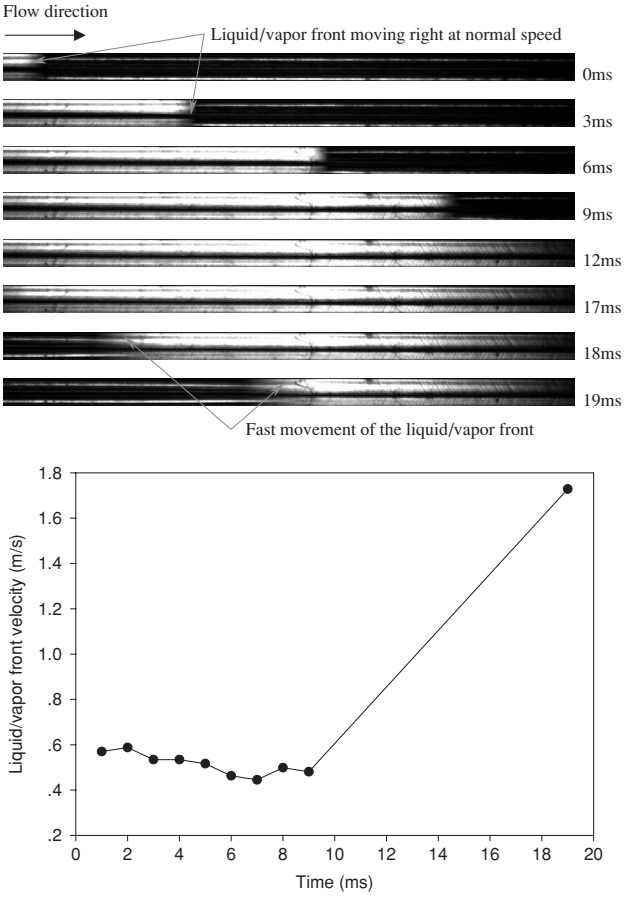

Figure 10. A comparison of the normal vapor/liquid front traveling velocity and the fast traveling velocity pushed by the merged bubble for channel 10.

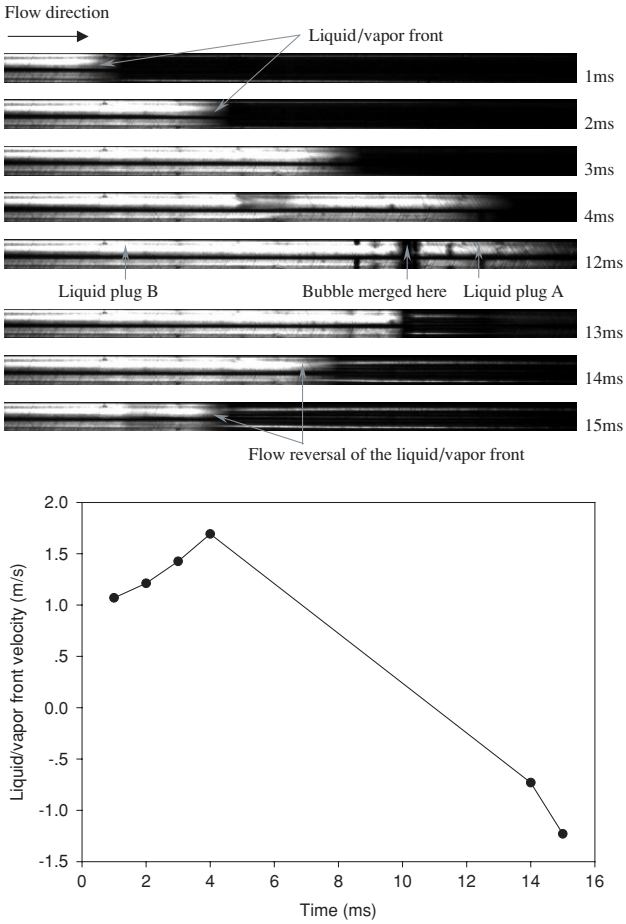

Figure 11. Flow reversal velocity of the separated liquid plug.

using deionized water as the working fluid and found that the majority of the first bubbles occurred on the channel bottom wall, though a few bubbles did appear on the side walls. Bubbles experience growth before departing into the liquid flow. The detached bubbles move to the downstream plenum.

In this paper, we found that the paired or triplet bubbles were always nucleated simultaneously in, or very close to, the channel corners at the same cross section. After nucleation, the group bubbles maybe in a stationary state or travel a very short distance, then merge together at the same cross section. Once a bubble coalesces, the sharp expansion of the merged bubble separates a single liquid plug into two parts, which are pushed out of the flow field view quickly. The whole process takes place in milliseconds.

*Transient liquid film evaporation stage (*22 ms $< t <$ 47 ms *in figure 5).* Following the above substage, all microchannels switch to the transient annular flow (flow pattern D in figure 6), corresponding to the transient liquid film evaporation stage. The black image indicates the vapor phase. While the parallel white lines represent the liquid film that accumulated in the channel corners drawn by the surface tension effect. Carefully checking the successive images frame-by-frame identifies the parallel white lines becoming darker and darker versus time, indicating that the liquid film in the channel

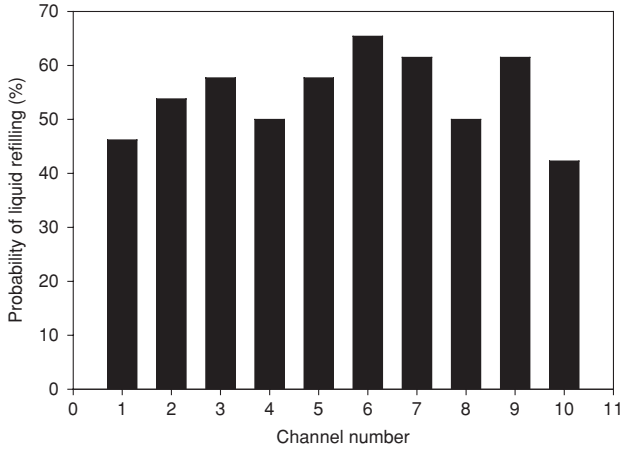

Figure 12. Probability of liquid refilling for each microchannel, statistic analysis performed for 26 successive full cycles.

corners becomes thin versus time. Such a transient liquid film evaporation stage is sustained until $t = 47$ ms at which some of the white lines totally disappear and the microchannels are ready to refill with fresh liquid for the next cycle. It is noted that the present 'transient liquid film evaporation' is for the annular flow, which is different from the term defined for the elongated bubble flow by Thome [19].

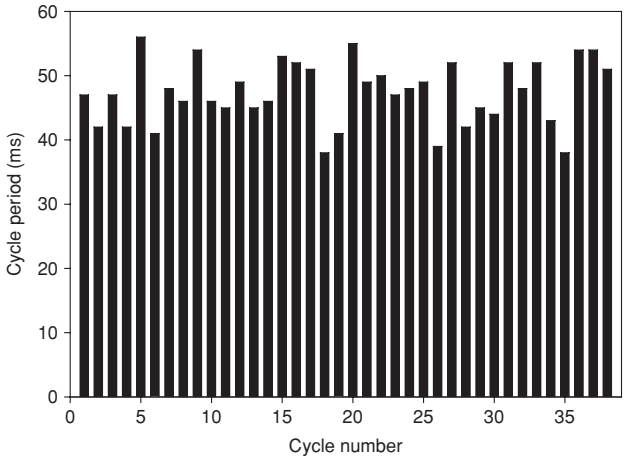

Figure 13. Cycle periods for different successive cycles.

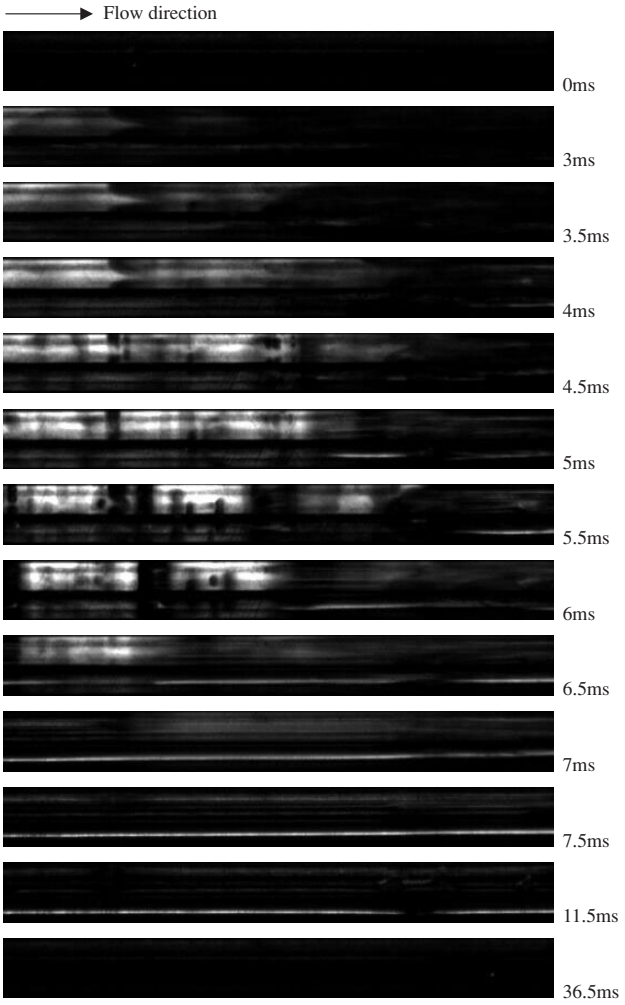

Figure 14. Transient flow pattern for channel 6 for a full cycle ($T_{in} = 24.7$ °C, $\Delta P = 30.84$ kPa, $G = 64.8$ kg m^{-2} s^{-1}, $q =$ 166.0 kW m^{-2}, $x_e = 1.1496$, $Re = 37.7$, cycle period = 36.5 ms).

3.2.2. Liquid refilling and cycle period behaviors. It is observed that in the selected flow field view only some of the microchannels are refilled by the fresh incoming liquid from the channel entrance for a specific cycle. However, if a specific microchannel is not refilled by the liquid in the current cycle, it may be refilled with liquid in the next cycle. We performed a statistical analysis on the liquid refilling for all the microchannels for successive 26 full cycles. The probability of liquid refilling for each channel is defined as the cycle numbers for which liquid refilling occurs divided by the 26 full cycles. As shown in figure 12 it is seen that the liquid refilling probabilities are not uniform for all the channels. Generally the side channels, such as channels 1, 2, 10, have the relatively lower liquid refilling probabilities than those of the center channels such as channels 4–8. It is interesting to note that such distributions roughly satisfy the parabola shape. A lot of factors influence the liquid refilling probabilities: the inlet and outlet fluid collectors, the silicon chip temperature field, the small pressure variations among different channels in milliseconds that could not be detected by the fluid pressure sensors etc.

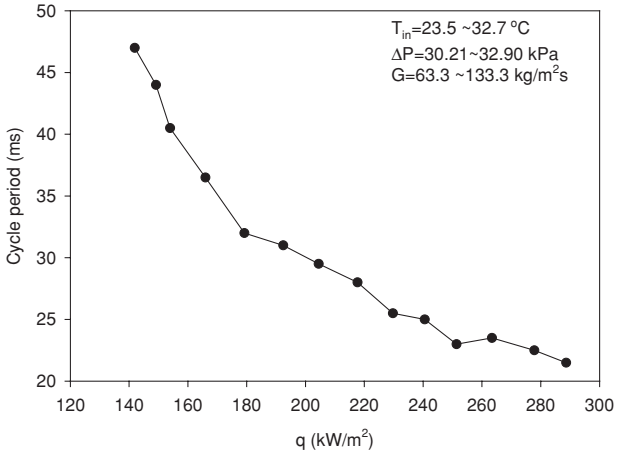

Figure 15. Decreased cycle periods with the increasing heat fluxes.

The cycle periods versus cycle numbers are illustrated in figure 13. It is seen that indeed all microchannels repeat the transient flow patterns periodically. The average cycle period is 47.5 ms, with the most cycles having the cycle periods from 40 to 50 ms.

3.3. Transient flow patterns and boiling phenomenon at high exit vapor mass quality

Another run with a similar pressure and inlet temperature to those in figure 5, but with a higher heat flux up to 166.0 kW m^{-2} is shown in figure 14, using six channels instead of the ten microchannels. The corresponding mass flux is 64.8 kg m^{-2} s^{-1}, the liquid Reynolds number is 37.7 and the mean exit vapor mass quality is 1.1496. Because the liquid front only reaches the front part of the microchannels in the selected flow field view, only a half-length of the flow field view is used.

With the mean exit vapor mass quality larger than unity (slightly superheated outlet vapor), the microchannels also repeat the transient flow patterns. As shown in figure 14, the image at $t = 0$ ms is the end of the previous cycle, $0 < t < 4$ ms is the liquid refilling stage without apparent bubble nucleation, 4 ms $< t <$ 6.5 ms is the bubble nucleation, growth and coalescence stage, 6.5 ms $< t <$ 36.5 ms is the transient annular flow stage, which covers 83% of the full cycle period. It is seen that by increasing the heat fluxes, the first two

substages are shorter, but the transient annular flow sustains a larger percentage of a full cycle period.

Even though the mean exit vapor mass quality is so high (corresponding to high heat flux), bubble nucleation, growth and coalescence can still be identified as shown at $t = 5.0$, 5.5, 6.0 and 6.5 ms, which process quickly. In the transient annular flow stage, the horizontal parallel white lines become gradually dimmer and dimmer versus time, indicating that the liquid film that was drawn to the channel corners become less and less, until the fully dried-out (fully dark images) state is reached.

In the present study, it is found that the heat flux is the major parameter that affects the cycle period, which expresses how fast the transient flow takes place. For the following data ranges, inlet temperatures of 23.5–32.7 °C, pressure drops of 30.2–32.9 kPa, mass fluxes of 63.4–133.3 kg m^{-2} s^{-1}, the cycle periods are decreased from 47 ms to 21 ms by increasing the heat flux, indicating that high heat flux shortens the cycle periods, as shown in figure 15.

3.4. Silicon chip temperature distributions

The conventional boiling curves are obtained by plotting the wall temperatures or superheats against the heat fluxes under the fixed mass fluxes. The wall superheat is defined as the mean wall temperature minus the saturated temperature of the fluid. The present experiments were performed by gradually increasing the heat flux under fixed pressure drop over the microchannels. The general trend is that the mass fluxes are decreased and the heated chip wall temperatures are increased

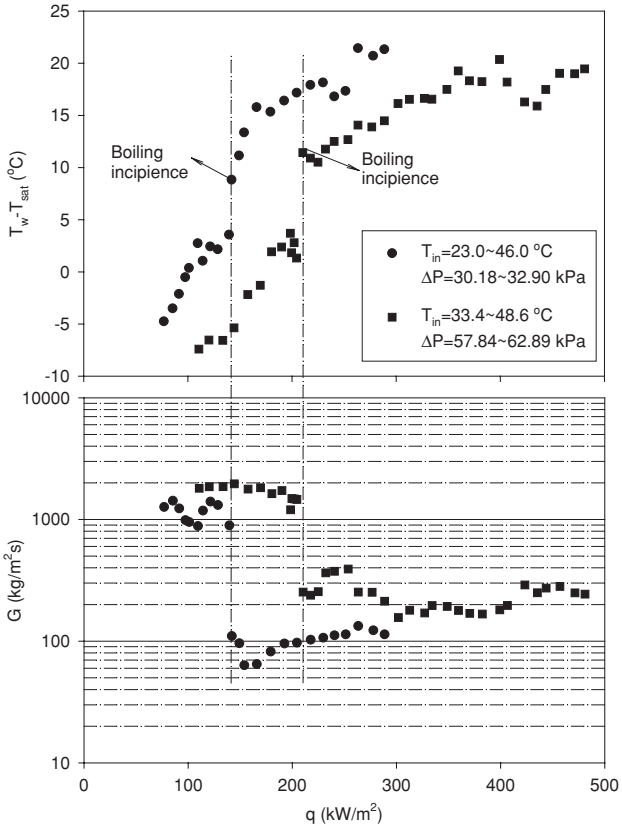

Figure 16. Chip wall superheats and mass fluxes versus heat flux for two different pressure drops.

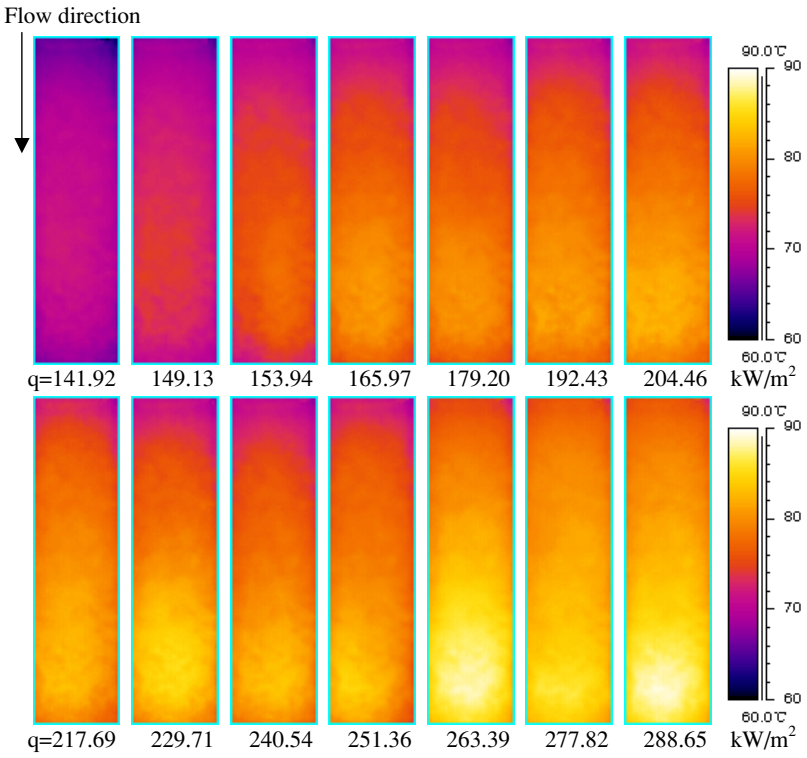

Figure 17. Color IR image showing the chip temperature field versus heat flux ($T_{in} = 23.0$–32.7Δ, $\Delta P = 30.21$–32.90 kPa, $G = 63.3$–133.3 kg m^{-2} s^{-1}).

(This figure is in colour only in the electronic version)

by increasing the heat fluxes. Boiling curves and mass fluxes are plotted in figure 16 for two different pressure drops of 30 kPa and 60 kPa. The boiling incipiencies distinguish the single-phase liquid flow from the transient two-phase flow, and are identified as the steep jump of the mass flux from a higher value to a lower value. In the single-phase liquid flow region, the mass fluxes are not varied by increasing the heat flux. However, the mean wall superheat is negative and is increased by increasing the heat fluxes. Boiling incipiencies take place at wall superheats of 3 to 10 °C for the pressure drops of 30 to 60 kPa. Beyond the heat flux at the boiling incipience, the mass fluxes show a slight increase versus the heat fluxes for lower pressure drops. The higher pressure drops such as 60 kPa result in the mass fluxes oscillating versus heat fluxes, due to the very complicated flow and heat transfer mechanism in parallel microchannels. It is found that under extremely high heat fluxes such as 400 kW m^{-2}, the wall superheats ($T_w - T_{sat}$) do not vary much, indicating that the bubble nucleation mechanism has little influence on the heat transfer.

The chip temperature distributions depend on the chip design, the mass flux and the heat fluxes. The optical system incorporating the microscope and the high-speed camera detects the transient flow patterns in all microchannels, which affect the chip temperatures. Even though the quantitative relationship between the transient flow patterns and the chip temperature distributions is difficult to establish at this stage, the present paper relates the transient flow patterns with the chip wall temperatures qualitatively. Because the maximum data-recording rate of the infrared radiator (IR) image system is only 50 images per second, the measured chip temperatures cannot follow the fast flow pattern transitions inside the microchannels. Besides, the silicon wall thickness (thermal inertia) flattens the chip temperature variations versus time. However, the spatially varied chip temperatures in the whole heating area, which are related to the liquid and vapor phase distributions inside all the microchannels, can be detected clearly, from the time statistical point of view on a millisecond scale.

The conventional boiling heat transfer provides a uniform wall temperature field due to the large heat transfer coefficients and the saturated fluid temperature. One may be concerned with the uniformity of the heated chip wall temperature field corresponding to the transient flow patterns in milliseconds. The measured chip surface temperatures show non-uniform temperature distributions, which is not as expected. The spatially varied temperatures are due to the uneven liquid refilling probabilities for different channels, and the uneven probabilities that were immersed in the liquid phase over all microchannels. From the real application point of view, the chip temperature gradient is an important issue to be considered for a high heat flux evaporator.

Figure 17 shows the IR color images demonstrating the chip temperature field for the whole selected heating area of 16 mm × 4.2 mm. The pressure drops over the microchannels are around 30 kPa, at which the mass fluxes are varied from 63.3 kg m^{-2} s^{-1} to 133.3 kg m^{-2} s^{-1}. The general trend is the increased temperatures with the increasing heat fluxes. Each image shows the non-uniform chip wall temperatures, especially in the flow length direction (from top to bottom). The maximum chip surface temperature is still 89.4 °C, even though the heat flux is high, up to 288.65 kW m^{-2}, and the mass flux is only 110 kg m^{-2} s^{-1}, demonstrating the large two-phase cooling capabilities in microchannels.

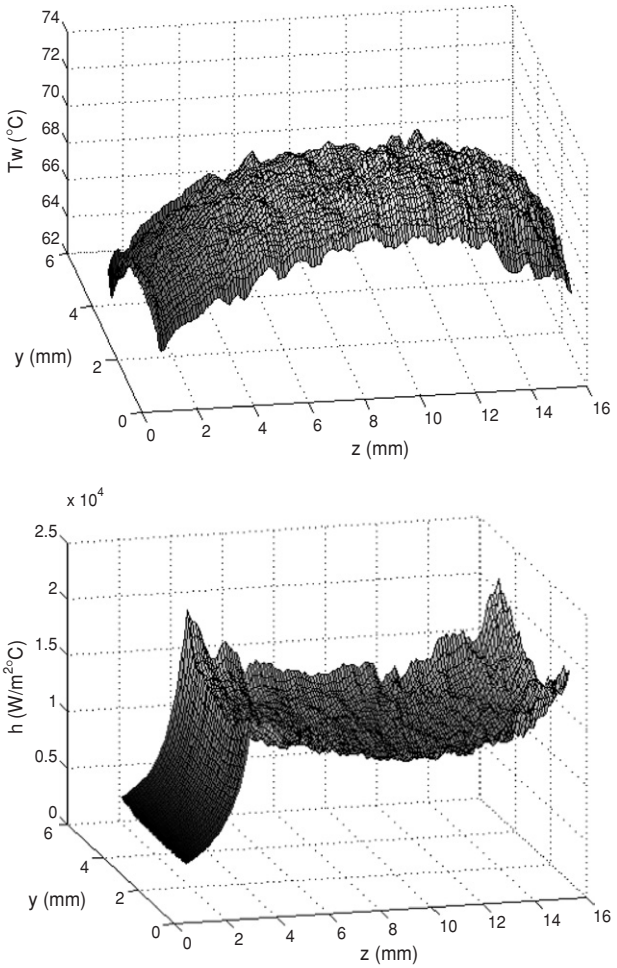

Figure 18. Chip wall temperature and heat transfer coefficient distributions ($T_{in} = 30.8$ °C, $\Delta P = 30.41$ kPa, $G = 110.1$ kg m^{-2} s^{-1}, $q = 141.92$ kW m^{-2}, $x_e = 0.5268$, $Re = 65.2$).

A two-dimensional (y- and z-coordinates) chip temperature and heat transfer coefficient distributions of the thin film heating area are illustrated in figure 18, with the same operating parameters as that in figure 5. It is seen from figure 18 that: (1) The chip temperatures are indeed non-uniform. The temperature differences in the whole heating area are about 6 °C, with the lower temperatures in the inlet, outlet and the four margin regions. (2) The lower, smooth but increased temperatures in the entrance region (corresponding to the single-phase liquid region, based on the energy conservation equation (4)) are caused by the greater possibility of the channel entrance part immersed in the liquid. (3) The chip temperatures in the majority of the chip heating area display spatial variation behavior, which may be caused by the transient flow patterns. The microchannels are flushed by the liquid or the vapor phases alternatively. (4) The lower temperatures at the margins are caused by the thermal conduction of the silicon wall at the interface between the heated area and the unheated area.

4. Conclusions

We performed the boiling heat transfer experiment in ten parallel microchannels with hydraulic diameters of 155.4 μm using acetone as the working fluid at high heat fluxes. The conclusions are summarized as follows:

- All microchannels display the transient flow pattern behavior in milliseconds.
- A full cycle can be subdivided into three substages: liquid refilling stage, bubble nucleation, growth and coalescence stage and transient liquid film evaporation stage. At the end of each cycle, the microchannels are always partially or totally dried out.
- Four flow patterns were observed: flow pattern A (liquid plug/vapor slug flow), flow pattern B (bubble slug entrained in a liquid plug), flow pattern C (paired or triplet bubbles entrained in a liquid plug) and flow pattern D (transient annular flow).
- It is observed that paired or triplet bubbles are always nucleated simultaneously in, or very close to, the channel corners at the same cross section. The group bubbles will experience the growth and coalescence process in milliseconds. Once the bubbles are merged, the quick energy release from the metastable superheated liquid to the vapor causes a sharp pressure increase, separating the single liquid plug into two parts, which are pushed out of the flow field view quickly in the order of 1 ms. The separated liquid plugs moving downstream and upstream may have the velocities three times than that of the normal liquid plug.
- Carefully checking a set of successive images demonstrates that the liquid film accumulated in the channel corners becomes darker and darker versus time, indicating that the liquid film becomes less and less in the transient annular flow stage.
- The statistical analysis shows that the occurrence probabilities of the four flow patterns satisfy the statistical principle for successive cycles.
- Based on the present chip design, the center channels have a greater probability of liquid refilling than the side channels. The microchannels display the quasi-cycle behaviors with the cycle periods a little oscillating over the averaged value.
- The measured chip temperatures show non-uniform behavior, which is not as expected. The majority of the heated area has spatial variation distributions due to the liquid and vapor phases alternately passing through the channels. The entrance region has smooth but increased temperatures due to a greater possibility that it was immersed in the liquid.

Acknowledgments

This work is supported by the National Natural Science Foundation of China (50476088), Natural Science Foundation of Guangdong Province (32700) and the Science and Technology Development Foundation of Guangdong Province (33103).

References

[1] Qu W and Mudawar I 2002 Prediction and measurements of incipient boiling heat flux in microchannel heat sinks *Int. J. Heat Mass Transfer* **45** 3933–45
[2] Kandlikar S G 2002 Fundamental issues related to flow boiling in minichannels and microchannels *Exp. Therm. Fluid Sci.* **26** 389–407
[3] Kandlikar S G 2004 Heat transfer mechanisms during flow boiling in microchannels *ASME J. Heat Transfer* **126** 8–16
[4] Thome J R 2004 Boiling in microchannels: a review of experiment and theory *Int. J. Heat Fluid Flow* **25** 128–39
[5] Kawahara A, Chung P M-Y and Kawaji M 2002 Investigation of two-phase flow pattern, void fraction and pressure drop in a microchannel *Int. J. Multiph. Flow* **28** 1411–35
[6] Chen I Y, Yang K S, Chang Y J and Wang C C 2001 Two-phase pressure drop of air–water and R-410A in small horizontal tubes *Int. J. Multiph. Flow* **27** 1293–9
[7] Zhao T S and Bi Q C 2001a Co-current air–water two-phase flow patterns in vertical triangular microchannels *Int. J. Multiph. Flow* **27** 765–82
[8] Triplett K A, Ghiaasiaan S M, Abdel-Khalik S I and Sadowski D L 1999a Gas–liquid two-phase flow in microchannels: 1. Two-phase flow pattern *Int. J. Multiph. Flow* **25** 377–94
[9] Feng Z P and Serizawa A 1999 Visualization of two-phase flow patterns in an ultra-small tube *Proc. 18th Multiphase Flow Symposium of Japan (Suita Osaka, 15–16 July)* pp 33–6
[10] Jiang L N and Wong M 2001 Forced convection boiling in a microchannel heat sink *J. Microelectromech. Syst.* **19** 80–7
[11] Peles Y P, Yarin L P and Hetsroni G J 2001 Steady and unsteady flow in a heated capillary *Int. J. Multiph. Flow* **27** 577–98
[12] Hetsroni G, Mosyak A, Segal Z and Pogrebnyak E 2003 Two-phase flow patterns in parallel microchannels *Int. J. Multiph. Flow* **29** 341–60
[13] Wu H Y and Cheng P 2003 Visualization and measurements of periodic boiling in silicon microchannels *Int. J. Heat Mass Transfer* **46** 2603–14
[14] Xu J L, Zhou J J and Gan Y H 2005 Static and dynamic flow instability of a parallel microchannel heat sink at high heat fluxes *Energy Convers. Manage.* **46** 313–34
[15] Hetsroni G, Mosyak A, Segal Z and Ziskind G 2002 A uniform temperature heat sink for cooling of electronic devices *Int. J. Heat Mass Transfer* **45** 3275–86
[16] Bennett G A and Briles S D 1989 Calibration procedure developed for IR surface-temperature measurements *IEEE Trans. Compon. Hybrids Manuf. Technol.* **12** 690–5
[17] Hapke I, Boye H and Schmidt J 2000 Onset of nucleate boiling in minichannels *Int. J. Therm. Sci.* **39** 505–13
[18] Yaws C L 1999 *Chemical Properties Handbook* (New York: McGraw-Hill)
[19] Thome J R, Dupont V and Jacobi A M 2004 Heat transfer model for evaporation in microchannels: 1. Presentation of the model *Int. J. Heat Mass Transfer* **47** 3375–85
[20] Peng X F and Wang B X 1993 Forced convection and flow boiling heat transfer for liquid flowing through microchannels *Int. J. Heat Mass Transfer* **36** 3421–7
[21] Peng X F and Wang B X 1994 Evaporation space and fictitious boiling for internal evaporation of liquid *Sci. Found. China* **2** 55–9